Identification of alternative protein targets of glutamate-ureido-lysine associated with PSMA tracer uptake in prostate cancer cells

Martin K. Bakht[a,b,c,d,e,f,1], John J. Hayward[a,1], Farsheed Shahbazi-Raz[a,1], Magdalena Skubal[g], Ryo Tamura[g], Keith F. Stringer[b,h], Daniel Meister[a], Varadha Balaji Venkadakrishnan[d,e,f], Hui Xue[i], Adam Pillon[b], Mathew Stover[b], Adam Tronchin[b], Bre-Anne Fifield[b], Lavleen Mader[a], Sheng-Yu Ku[d,e], Gi Jeong Cheon[c,j], Keon Wook Kang[c,j], Yuzhuo Wang[i], Xuesen Dong[i], Himisha Beltran[d,e,f], Jan Grimm[g,k,l], Lisa A. Porter[b,2], and John F. Trant[a,2]

[a]Department of Chemistry and Biochemistry, University of Windsor, Windsor, ON N9B 3P4, Canada; [b]Department of Biomedical Sciences, University of Windsor, Windsor, ON N9B 3P4, Canada; [c]Department of Nuclear Medicine, Seoul National University College of Medicine, Seoul 03080, Korea; [d]Department of Medical Oncology, Dana Farber Cancer Institute, Boston, MA 02215; [e]Department of Medicine, Harvard Medical School, Boston, MA 02115; [f]Broad Institute of MIT and Harvard, Cambridge, MA 02142; [g]Molecular Pharmacology Program, Memorial Sloan Kettering Cancer Center, New York, NY 10065; [h]Department of Pathology, Cincinnati Children's Hospital Medical Center, Cincinnati, OH 45229; [i]Vancouver Prostate Centre, University of British Columbia, Vancouver, BC V6H 3Z6, Canada; [j]Cancer Research Institute, Seoul National University, Seoul 03080, Korea; [k]Department of Radiology, Memorial Sloan Kettering Cancer Center, New York, NY 10065; and [l]Pharmacology Program, Weill Cornell Medical College, New York, NY 10065

Edited by Arul Chinnaiyan, Michigan Center for Translational Pathology, University of Michigan Medical School, Ann Arbor, MI; received December 14, 2020; accepted November 17, 2021

Prostate-specific membrane antigen (PSMA) is highly overexpressed in most prostate cancers and is clinically visualized using PSMA-specific probes incorporating glutamate-ureido-lysine (GUL). PSMA is effectively absent from certain high-mortality, treatment-resistant subsets of prostate cancers, such as neuroendocrine prostate cancer (NEPC); however, GUL-based PSMA tracers are still reported to have the potential to identify NEPC metastatic tumors. These probes may bind unknown proteins associated with PSMA-suppressed cancers. We have identified the up-regulation of PSMA-like aminopeptidase NAALADaseL and the metabotropic glutamate receptors (mGluRs) in PSMA-suppressed prostate cancers and find that their expression levels inversely correlate with PSMA expression and are associated with GUL-based radiotracer uptake. Furthermore, we identify that NAALADaseL and mGluR expression correlates with a unique cell cycle signature. This provides an opportunity for the future study of the biology of NEPC and potential therapeutic directions. Computationally predicting that GUL-based probes bind well to these targets, we designed and synthesized a fluorescent PSMA tracer to investigate these proteins in vitro, where it shows excellent affinity for PSMA, NAALADaseL, and specific mGluRs associated with poor prognosis.

PSMA | prostate cancer | glutamate-ureido-lysine | molecular imaging | PET

In 2021, 248,530 American men will be diagnosed with, and 34,130 will die from, prostate cancer. Although mortality has fallen 52% from its 1993 peak, prostate cancer remains a leading cause of cancer death (1). The use of positron emission tomography (PET) imaging for accurate diagnosis and localization of tumors has started to improve prostate cancer staging, enhancing patient management (2). Prostate-specific membrane antigen (PSMA), a cell surface protein expressed in the majority of prostate cancers, can be visualized by PET imaging employing radiolabeled antibodies. Next-generation imaging agents based on small molecule moieties, particularly the PSMA-targeting peptidomimetic glutamate-ureido-lysine (GUL), demonstrate superior pharmacokinetics (fast tumor uptake and rapid blood clearance) over radiolabeled PSMA antibodies (Fig. 1*A*) (3). The molecular mode of action of GUL-based probes, however, is not completely understood (4, 5). The leading clinical candidates are US Food and Drug Administration (FDA)–approved ^{68}Ga-PSMA-11 (Ga-GUL) (6), where the GUL head is conjugated to an acyclic hexadentate gallium ligand, and both ^{18}F-PSMA-1007 (F-GUL) (7) and FDA-approved ^{18}F-DCFPyL (8), where GUL is connected to a pseudopeptide functionalized with an ^{18}F isotope (Fig. 1*A*) (9, 10).

PSMA, a type II glutamate carboxypeptidase encoded by the folate hydrolase 1 gene (*FOLH1*) (11, 12), is expressed primarily in the duodenum, small intestine, nervous system, salivary gland, and prostate (13). It modulates glutamate signaling induced by the metabotropic glutamate receptor (mGluR) pathway (14), cleaving glutamate from both dietary folic acid and the

Significance

Glutamate-ureido-lysine (GUL) probes are specific for prostate-specific membrane antigen (PSMA), overexpressed by most prostate cancers. This antigen can be lost as the cancer progresses. Recent reports have indicated that GUL probes can still identify these PSMA-negative tumors, indicating that the expression of alternative PSMA-like proteins may change during disease progression. In this study we identified two such candidate protein targets, NAALADaseL and mGluR8, by using a combined computational chemistry, data mining, molecular biology, radiochemistry, and synthetic chemistry approach. This work consequently prepares the groundwork for developing specific probes that can identify this progression, indicates directions for neuroendocrine prostate cancer research, and highlights the utility of a multidisciplinary approach for the rapid identification of unidentified proteins interacting with diagnostic probes.

Author contributions: M.K.B., F.S.-R., G.J.C., K.W.K., J.G., L.A.P., and J.F.T. designed research; M.K.B., J.J.H., F.S.-R., M.S., R.T., K.F.S., D.M., V.B.V., H.X., A.P., M.S., A.T., B.-A.F., L.M., S.-Y.K., and Y.W. performed research; F.S.-R., K.F.S., D.M., L.A.P., and J.F.T. contributed new reagents/analytic tools; M.K.B., J.J.H., F.S.-R., D.M., X.D., H.B., L.A.P., and J.F.T. analyzed data; M.K.B., F.S.-R., K.F.S., and V.B.V. contributed to visualization; S.-Y.K., G.J.C., K.W.K., X.D., J.G., L.A.P., and J.F.T. acquired funding; G.J.C., K.W.K., H.B., J.G., L.A.P., and J.F.T. supervised the study; L.A.P. and J.F.T. were responsible for project administration; M.K.B., J.J.H., F.S.-R., D.M., B.-A.F., L.A.P., and J.F.T. wrote the paper; and M.K.B., J.J.H., F.S.-R., M.S., R.T., K.F.S., D.M., V.B.V., H.X., A.P., B.-A.F., S.-Y.K., G.J.C., K.W.K., X.D., H.B., J.G., L.A.P., and J.F.T. edited the paper.

The authors declare no competing interest.

This article is a PNAS Direct Submission.

This article is distributed under Creative Commons Attribution-NonCommercial-NoDerivatives License 4.0 (CC BY-NC-ND).

[1]M.K.B., J.J.H., and F.S.-R. contributed equally to this work.

[2]To whom correspondence may be addressed. Email: lporter@uwindsor.ca or j.trant@uwindsor.ca.

This article contains supporting information online at http://www.pnas.org/lookup/suppl/doi:10.1073/pnas.2025710119/-/DCSupplemental.

Published January 21, 2022.

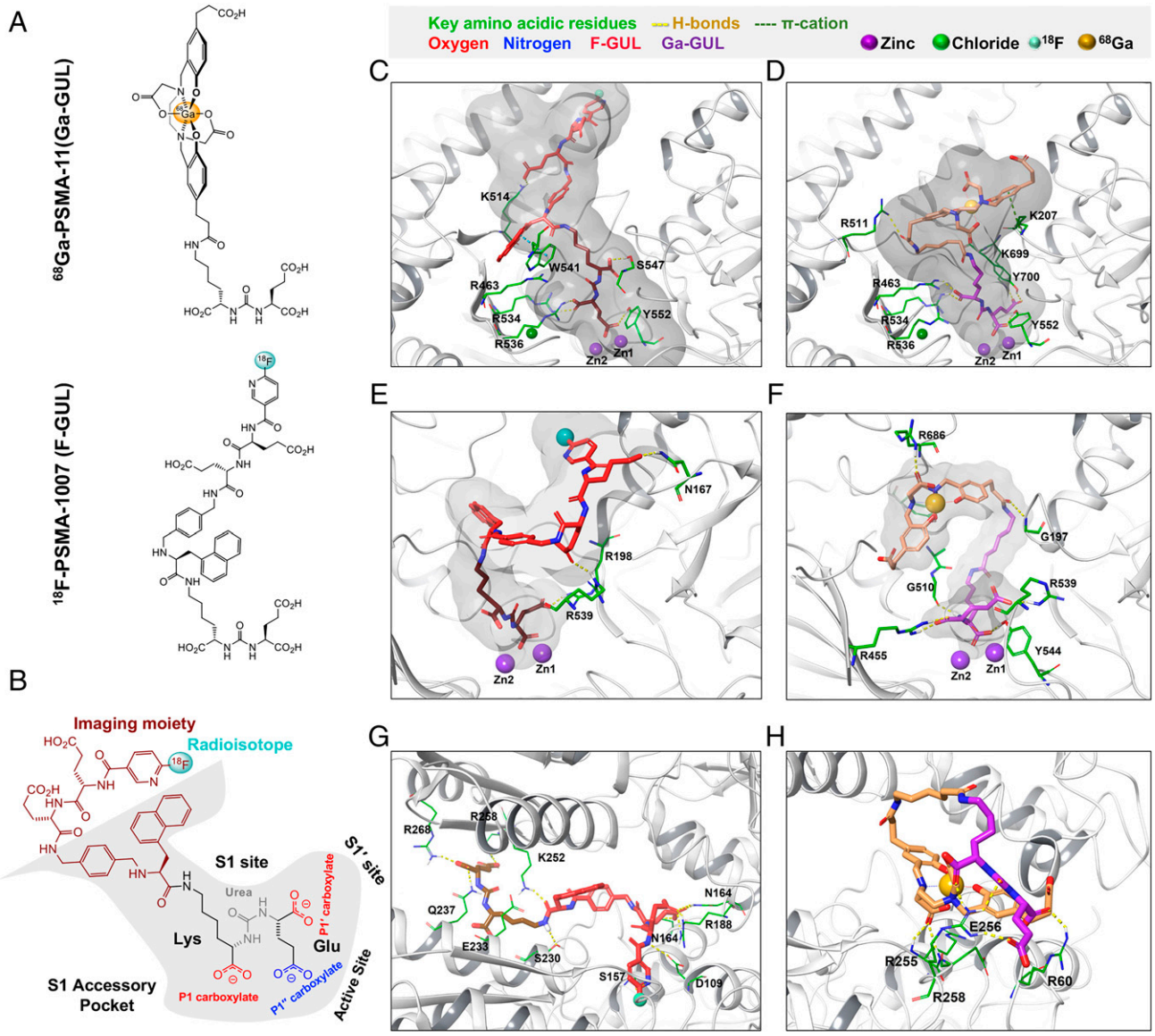

Fig. 1. Structure of clinical PSMA probes and their binding modes within the PSMA, NAALADaseL, and mGluR8 active sites. (*A*) Structure of Ga-GUL (*Top*) and F-GUL (*Bottom*). (*B*) F-GUL within the PSMA active site, showing the different regions of the active site and the substructure nomenclature of the probe. Computational modeling of (*C*) F-GUL and (*D*) Ga-GUL within the PSMA active site (*2XEG*), (*E*) F-GUL and (*F*) Ga-GUL within the NAALADaseL active site (*4TWE*), and (*G*) F-GUL and (*H*) Ga-GUL within the mGluR8 active site (*6BSZ*). The imaging moieties are shown in red (F-GUL) and beige (Ga-GUL) with the GUL moiety in brown (F-GUL) and purple (Ga-GUL). Key residues which form strong interactions—H bonds (yellow dashed lines) and π cation (green dashed line)—are highlighted in green, and zinc, chlorine, gallium, and fluorine atoms are spheres colored purple, green, blue, and orange, respectively.

neurotransmitter *N*-acetyl-L-aspartyl-L-glutamate (NAAG). PSMA overexpression is a hallmark of prostate cancer including metastatic castration-resistant prostate adenocarcinoma (15, 16). Despite this, both immunohistochemical and genomic data have demonstrated that PSMA is expressed at only very low levels, if at all, in neuroendocrine prostate cancer (NEPC) (17, 18), an aggressive form of androgen receptor (AR)–independent prostate cancer with exceedingly high mortality rates (18). While de novo NEPC is rare, this hard-to-treat phenotype can emerge as a prostate cancer resistance mechanism to AR-targeted therapies, shedding the PSMA biomarker concurrent with a down-regulation of the AR (18–20).

Paschalis et al. (21) reported PSMA expression can be heterogeneous within tumors of a single patient, so GUL-based radiotracers would still delineate PSMA-positive portions of tumors. However, if other portions of the tumor or metastatic colonies were PSMA-negative, these would not be observed. Similarly, GUL-based radiotracers are not expected to be useful for imaging PSMA-negative prostate tumors such as NEPC. A less specific agent, ^{18}F-fluorodeoxyglucose, which exploits cancer cells' increased glucose uptake, is often used for NEPC imaging as in small cell lung cancer (22, 23).

Unexpectedly, Iravani et al. demonstrated that GUL-based imaging can identify immunohistochemistry-validated PSMA-negative metastatic tumors despite the tumor's PSMA-negativity (24). Similarly, another recent study by Derlin et al. showed that neuroendocrine marker profiles do not reliably predict the outcome of PSMA-targeted radioligand therapy (25). Furthermore, although PSMA expression is correlated with GUL radioligand uptake (26), GUL-based PSMA tracers have also resulted in false

positive interpretations among patients with a history of radiotherapy (27). Together, the evidence suggests that GUL interacts fortuitously with other proteins that are up-regulated in cancer relative to surrounding healthy tissue. Identifying these targets and determining whether they are indicative of more aggressive subsets of prostate cancer is a pressing clinical goal.

We hypothesized that PSMA-like proteins such as NAALADaseL and mGluRs, other type II transmembrane peptidases associated with glutamate signaling, may be responsible for positive results found with GUL-based tracers in NEPC and NE-like prostate cancer. In this study, we investigated this question with a cross-disciplinary combination of computational chemistry, synthesis, molecular biology, and histochemical application of a GUL-incorporating fluorescent tracer, in vitro Ga-GUL radioligand uptake measurements, mining of clinical data, in vitro overexpression and knockdown of the suspected proteins, and in vivo patient-derived xenograft (PDX) models.

Results and Discussion

F-GUL and Ga-GUL Are Predicted to Have High Affinity for PSMA. GUL-based probes interact with three components of PSMA's active site: the zinc ions, the pharmacophore (S1′) site, and the hydrophobic S1 accessory pocket (Fig. 1*B*) (28). PSMA's active site hosts two Zn^{2+} ions, responsible for substrate cleavage (*SI Appendix*, Fig. S1*A*) (29, 30). The S1′ site, which is highly specific for glutamate moieties, determines substrate specificity (31). The large hydrophobic S1 accessory pocket, hosting the rest of the substrate, is far more promiscuous allowing for binding of both folate and NAAG (32).

To better understand probe–protein interactions, in silico docking studies were performed between the two GUL radiolabels and a computationally relaxed PSMA protein (Protein Data Bank [PDB] ID 2XEG) (33) (Movies S1 and S2). Although the ligands' conformations differ (Fig. 1 *C* and *D*), both share similar interactions with the same Tyr552 active site residue and the Zn^{2+} ions (*SI Appendix*, Fig. S1*B*), but F-GUL does not extend into the S1′ site like Ga-GUL does. Both probes are predicted to have high affinity for PSMA, with induced-fit docking scores around −15 kcal/mol (Table 1). Computed binding modes are consistent with the previously hypothesized interactions (31, 34, 35).

The P1″ glutamate carboxylate moiety of F-GUL (Fig. 1*C*) forms strong interactions with the zincs (2.06 and 1.95 Å) and a strong hydrogen bond (2.06 Å) to the phenolic H of the S1′ Tyr552. A major structural feature of PSMA's S1 site is the accessory pocket, whose entrance lid comprises three arginine residues (Arg536, Arg534, and Arg463) that can flip open to accommodate larger molecules. The P1′ carboxylate of F-GUL is stabilized by H bonds with the residues Arg536 (1.73 Å) and Arg534 (1.67 Å), while the P1 carboxylate has a strong H bond interaction with nearby Ser547. The rigidity of the F-GUL linker enables the radiolabel-bearing moiety to remain inside the pocket. This results in a likely important π–π interaction with Trp541 and several H bonds with Lys514 (*SI Appendix*, Fig. S2*A*).

Ga-GUL's longer nine-atom linker chain enables it to enter deeper, properly occupying the S1′ pocket (Fig. 1*D*), engaging in H bonds with Lys699 (1.81 Å) and Tyr700 (1.85 Å) through the P1″ acid and Tyr552 (1.70 Å) through the P1′ acid. The P1 glutamate carboxylate forms an isosceles triangle interaction with 2.18 Å distances to both zinc ions. Ga-GUL's long linker forms H bonds with Arg511 and a key π-cation interaction with Lys207 that guides the probe into place (*SI Appendix*, Fig. S2*B*). This structural tour, consistent with the literature (36), gave us confidence in the binding mode of the probes. Consequently, we extended this approach to the two NEPC-suspect proteins.

Table 1. Docking scores for the probes with the target proteins from both rigid and induced docking models

		Docking score (kcal/mol)	
Receptor	Ligand	RRD score	IFD score
PSMA	Cy3-GUL	−12.93	−13.73
	Ga-GUL	−11.29	−13.10
	F-GUL	−11.66	−14.83
NAALADaseL	Cy3-GUL	−9.09	−10.83
	Ga-GUL	−1.69	−12.25
	F-GUL	−8.20	−12.91
mGluR8	Cy3-GUL	−8.15	−11.28
	Ga-GUL	−4.09	−6.64
	F-GUL	−7.67	−13.16

F-GUL and Ga-GUL Bind NAALADaseL and mGluR8. The GUL moiety in F-GUL binds to NAALADaseL in a manner reminiscent of the PSMA binding of Ga-GUL, occupying the S1′ pocket due to NAALADaseL's larger, more open pocket (Fig. 1*E* and Movie S3). F-GUL's P1″ glutamate carboxylate forms an H bond with Arg198, while the P1′ carboxylate bridges $Zn(1)^{2+}$ and $Zn(2)^{2+}$ at distances of 2.07 and 2.27 Å, respectively. The aromatic domains of F-GUL are positioned on the outer surface of the receptor, stabilized by a series of H bond interactions with Asn167 and Arg539 (*SI Appendix*, Fig. S2*D*). The carboxylates of Ga-GUL's glutamates adopt analogous positions (Fig. 1*F* and Movie S4), but the linker takes a very different path out of the active site through the wide channel (*SI Appendix*, Fig. S1*C*); Arg539–P1″ carboxylate, Arg455–P1′ carboxylate, and Gly510–ureido carbonyl H bonds hold the linker in conformation. The Ga-GUL P1′ carboxylate interacts with $Zn(1)^{2+}$ and $Zn(2)^{2+}$ at distances of 2.17 and 2.09 Å, respectively (*SI Appendix*, Fig. S2*E*). The subtly different structure clearly induces differences in conformation (*SI Appendix*, Fig. S1*C*), but docking scores predict both ligands to be excellent partners for the accommodating NAALADaseL (Table 1).

The mGluRs always self-assemble into homodimers in vivo. The probes were docked (without restrictions) to each of the eight mGluR homodimers but showed the best affinity for mGluR1, mGluR5, and mGluR8 (*SI Appendix*, Table S3). Curiously, the probes do not interact with the glutamate-binding active site of these proteins, which is far narrower than either PSMA's or NAALADaseL's; instead, they bind to the large intermonomer cleft (Fig. 1 *G* and *H* and Movies S5 and S6). Induced-fit docking predicts the best binding to mGluR5 and mGluR8, with scores on par with NAALADaseL and only slightly inferior to PSMA (Table 1 and *SI Appendix*, Table S3). The docking scores to the other mGluRs were lower (−5.2 to −11.5 kcal/mol) but remain favorable. Molecular dynamics simulations helped us understand the high docking score and the unusual binding mode of the probes with mGluR8, which we identified as being particularly relevant to NEPC (vide infra). Very little movement is observed within the binding cleft for either ligand: most structures fall within a 1 Å cluster adopting a common conformation (*SI Appendix*, Fig. S4) due to an extensive hydrogen bonding network that forms between the positively charged residues of the cleft and the negatively charged probes (*SI Appendix*, Figs. S5–S16). However, the two probes bind very differently despite both having strong affinity (*SI Appendix*, Fig. S1*D*), possibly due to the large size of the cleft. F-GUL (Fig. 1*G*) is particularly stable, adopting an extended conformation maximizing hydrogen bonding interactions between the glutamate and the highly positive interprotein region's residues Arg188 and Arg240 of one monomer and Ser157, Asn226, Lys252, Arg255, and Arg268 in the other (*SI Appendix*, Fig. S2*G*). Ga-GUL (Fig. 1*H*) forms far fewer interactions and instead folds

in on itself, held together by an intramolecular hydrogen bond, but it still interacts with Ser200, Gln237, and Asn186 of one monomer and Arg60 and Arg255 in the other. Both complexes are highly stabilized through these interactions making mGluR8 an exceptional potential molecular target (*SI Appendix*, Fig. S2*H*).

These data predict that both F-GUL and Ga-GUL will have strong affinity, comparable to PSMA, for both NAALADaseL and a subset of mGluRs. It is conceivable that these two protein classes are responsible for the GUL probes' efficacy in detecting PSMA-suppressed cancers; however, it is unknown whether these proteins are associated with NEPC.

Aminopeptidase NAALADaseL Is Elevated in NEPC and NE-Like Prostate Cancer. NAALADaseL, encoded by *NAALADL1*, has high sequence similarity to PSMA (*SI Appendix*, Fig. S3) (37). They share more than 90% structurally equivalent residues, with near-complete identity at the active site (*SI Appendix*, Fig. S3; PDB ID *2XEJ* and *4TWE*) (38). We examined the expression of NAALADaseL using the LTL331 PDX model of prostate cancer progression from adenocarcinoma to NEPC (Fig. 2*A*) (41). *NAALADL1* gene expression remains minimal during the effective treatment period but spikes as the tumor becomes resistant to therapy, and peak expression occurs when the tumor transitions to NEPC. This profile inversely correlates with that of *FOLH1* (Fig. 2*A*). We examined the relative expression of *FOLH1* and *NAALADL1* in the well-established cells lines of the DepMap 21Q3 dataset (n = 1,377) (39). *NAALADL1* gene expression is low in typical prostate cancer cell lines, while it is high in the human medullary thyroid carcinoma TT cell line (Fig. 2*B*). At the protein level, our preprogression LTL331 model is PSMA-positive and NAALADaseL-negative, while after progressing to a PSMA-negative NEPC form, we observe low, but detectable, NAALADaseL positivity (Fig. 2 *C* and *D*). The RNA-seq analysis of metastatic prostate cancer tumors also shows that *NAALADL1* expression rises during the transition to castration-resistant prostate cancer (CRPC) and can be significantly elevated in histopathologically confirmed NEPC (Fig. 2*E*). This trend is mirrored in the Dream Team patient dataset (Fig. 2*F*) (40). When ordering patients by increasing AR score, *NAALADL1* expression is lower, while PSMA expression (*FOLH1*) is higher; furthermore, NEPC score is strongly positively correlated with *NAALADL1* expression. As *NAALADL1* is elevated in low-PSMA prostate cancers with an NE-like gene signature (Fig. 2 *G* and *H*), these data are consistent with the computational supposition that NAALADaseL may be one target of the GUL probes on PSMA-suppressed cells.

mGluRs Are Up-Regulated during Progression to NEPC. The second class of proteins identified for investigation was the mGluRs, encoded by *GRM*s. While increased expression of mGluR2 has already been reported in PSMA-positive cancers (14), we observed a significant up-regulation in the expression of most mGluR family members during cancer progression from prostate adenocarcinoma (AdPC) to NEPC in our PDX mouse model (*SI Appendix*, Fig. S17) and in the NCIH660 cell line model of NEPC (Fig. 3*A*). Following castration, *GRM2*, *GRM3*, *GRM4*, and *GRM8* all become increasingly expressed as *FOLH1* expression down-regulates (*SI Appendix*, Fig. S17). Furthermore, their expression is strongly positively correlated to that of *SRRM4*, the archetypal biomarker of NEPC (*SI Appendix*, Fig. S18). Data mining the Memorial Sloan Kettering Cancer Center cohort (43) for prostate tumor survival identifies that high levels of *GRM1*, *GRM3*, *GRM4*, and especially *GRM5* and *GRM8*, are correlated with shorter times to biochemical recurrence, with *GRM8* showing the most significant effect (*SI Appendix*, Fig. S19). Further investigation revealed that high levels of *GRM8* expression are associated with a higher prevalence of metastatic cancer and higher Gleason scores (*SI Appendix*, Fig. S20). Our data indicate that expression levels of *GRM8* rise during the transition to CRPC and can be significantly elevated in histopathologically confirmed NEPC (Fig. 3*B*). Fig. 3*C* shows the expression of *FOLH1* and *GRM8* in the cell lines of the DepMap 21Q3 dataset (39). We have also determined that the TT cell line expresses high levels of *GRM8* making it a good biochemical positive control (Fig. 3*C*). In our LTL331 model, progression to NEPC, LTL331R, leads to higher mGluR8 levels than in the initial LTL331 AdPC PDX model (Fig. 3 *D* and *E*) (39).

Cyclin A1-CDK1/2 Activity in NEPC Is Associated with NAALADaseL and mGluR8 Expression. Fig. 3*F* shows a volcano plot of differential gene expression (DGE) analysis in *GRM8*-high (n = 5) vs. *GRM8*-low tumors (n = 5) in the Stand Up to Cancer/Prostate Cancer Foundation (SU2C/PCF) Dream Team Dataset 2019 (40). *GRM8*-high tumors suppressed typical AR-signaling markers such as *AR*, *FOLH1*, *KLK2/3*, and *NKX3-1*. *GRM8*-high samples express higher levels of *PCNA*, a marker of cell proliferation, and higher levels of *ENO2* (a marker of NEPC) than the *GRM8*-low samples. Kinase enrichment analysis (KEA) results (Fig. 3*G*) were generated by analyzing the up-regulated and down-regulated gene sets using Enrichr (42). A similar KEA on *NAALADL1*-high samples was performed. Two cyclin-dependent kinases (CDKs) including *CDK1* and *CDK2* were the most enriched kinase in the *GRM8*-high and *NAALADL1*-high cohorts (Fig. 3*H*). CDK1 and CDK2 both make a complex with Cyclin A and facilitate cell cycle progression at DNA synthesis and mitosis. Cyclin A expression is elevated in a variety of cancers (44), but its significance has not been investigated in NEPC. Looking at this from a different angle, we observed this same elevation of Cyclin A1 and CDK1/2 gene expression among pathologically confirmed NEPC tumors (*SI Appendix*, Fig. S21). Transcription changes in cyclin and CDK genes during progression from AdPC to NEPC in a series of PDX mice models are illustrated in *SI Appendix*, Fig. S22*A*. The nearest neighbors to *FOLH1* analysis in *SI Appendix*, Fig. S22*A* shows Cyclin A1 and E1 and their partners including CDK1 and CDK2 are among the farthest neighbors to *FOLH1*. Ongoing phase 2 clinical trials for management of CRPC have focused on strategies using CDK4/6 inhibitors such as palbociclib and abemaciclib (clinical trials identifiers NCT02905318 and NCT04408924). *SI Appendix*, Fig. S22*A* shows Cyclin D1 and CDK4/6 are not correlated with progression to NEPC while the elements of the Cyclin A1-CDK1/2 complex are differentially expressed in NEPC. The LNCaP-NE–like cell line also has elevated Cyclin A1 protein levels along with elevated mGluR8 and NAALADL1 (Fig. 3*I*). The heat map (Fig. 3*J*) shows that progression to NEPC is associated with up-regulation of *CDK1/2*, *CCNA1*, *GRM8*, and *NAALADL1*. As a preliminary exploration of the role of CDK1/2 activity in the proliferation of NEPC, our LNCaP models were treated with dinaciclib, a potent inhibitor of CDKs 1, 2, 5, and 9 (44). An enzalutamide (ENZ)-resistant LNCaP-NE–like cell line with an elevated level of Cyclin A1 showed a lower half-maximal inhibitory concentration (IC_{50}) than the ENZ-sensitive LNCaP–wild type (WT) (Fig. 3*K*). The identified sensitivity of NE-like LNCaP supports the feasibility of dinaciclib as an inhibitor of CDK1/2 for NEPC management; this result is worthy of future exploration. Likewise, *CCNA1*, *CDK1/2*, *PCNA*, *NAALADL1*, and *GRM8* expression are elevated in pathologically confirmed NEPC (Fig. 3*L* and *SI Appendix*, Figs. S23 and S24). Collectively, these data show that the mGluRs and NAALADaseL are clearly associated with the NEPC gene signature and correlate positively with Cyclin A1 and CDK1/2 expression. These data alone do not dissect causality, and it is possible that elevated expression of mGluR, NAALADaseL and Cyclin A1, CDK1/2 in NEPC are part of separate underlying mechanisms. However, these data are intriguing, and these molecular relationships deserve further investigation.

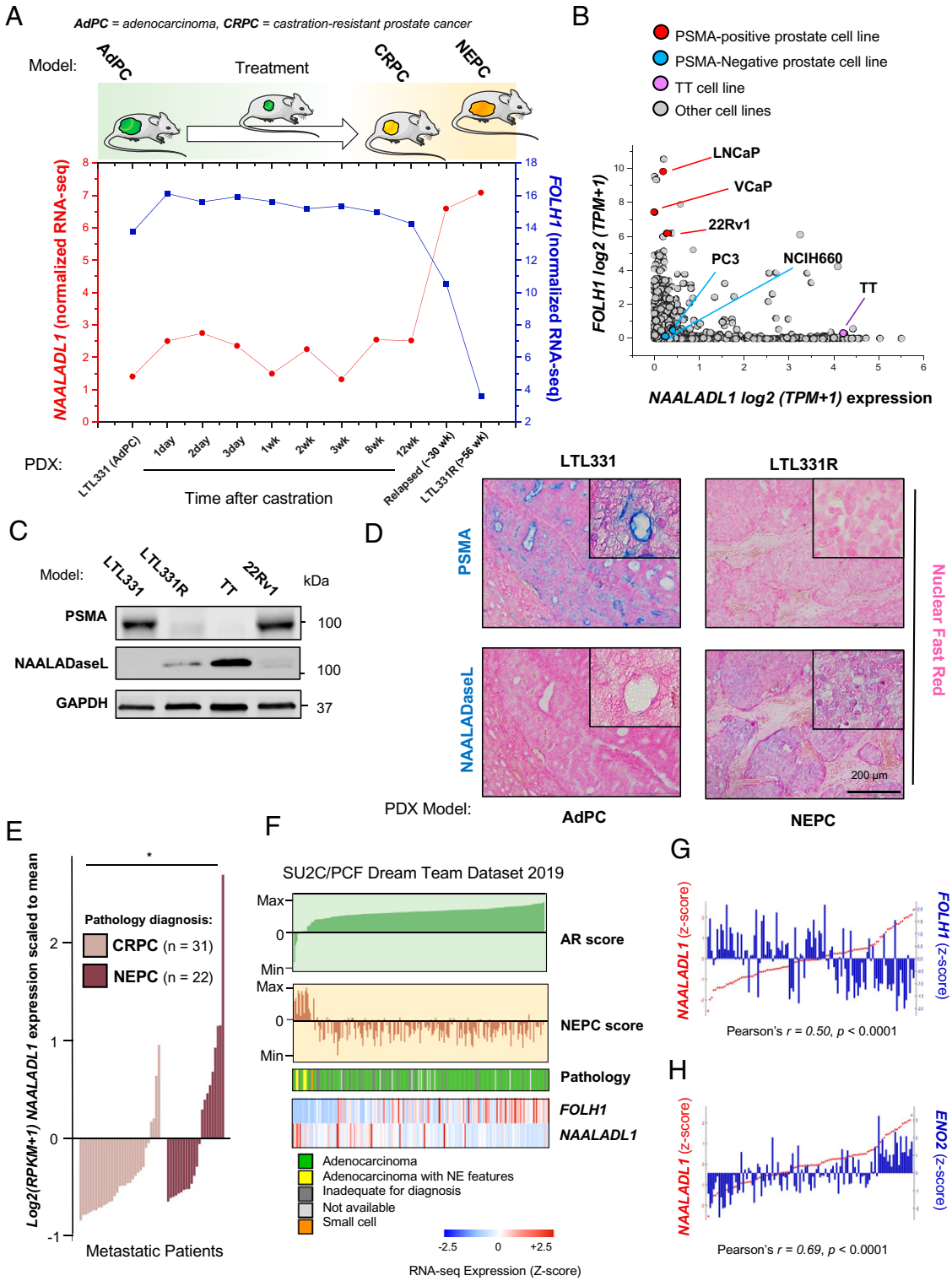

Fig. 2. Differential expression of *NAALADL1* in NEPC and NE-like PC as an alternative target for GUL ligands. (*A*) Schematic of our established PDX mice models of adenocarcinoma (AdPC) and NEPC and alteration of *FOLH1* and *NAALADL1* gene expression during the transition from AdPC to NEPC. (*B*) The expression of *FOLH1* and *NAALADL1* in well-established cells lines (n = 1,377) of DepMap 21Q3 dataset (39). (*C*) PSMA and NAALADaseL levels in LTL331 and LTL331R models were detected by immunoblotting. TT and 22Rv1 cell lines were used as NAALADaseL- and PSMA-positive control samples, respectively. (*D*) Tissue sections of LTL331 models stained with nuclear fast red to visualize cell nuclei and blue chromogenic substrate used for detection of PSMA and NAALADaseL. (*E*) *NAALADL1* gene expression level in different cohorts of metastatic prostate cancer samples. The expression levels are normalized to the mean of entire samples in the cohort (n = 155). (*F*) Evaluation of the expression of *FOLH1* and *NAALADL1* genes and their association with AR and NEPC scores in the SU2C/PCF Dream Team Dataset 2019 (40). The high levels of *NAALADL1* gene expression in AdPC are associated with both lower levels of *FOLH1* gene expression and higher levels of *ENO2* gene expression, the archetypal NE marker. (*G*) Pearson's correlation between *FOLH1* (blue) and *NAALADL1* (red) expression levels. (*H*) Pearson's correlation between *ENO2* (blue) and *NAALADL1* (red) expression levels among AdPC samples (n = 199) generated by R2: Genomics Analysis and Visualization Platform (http://r2.amc.nl).

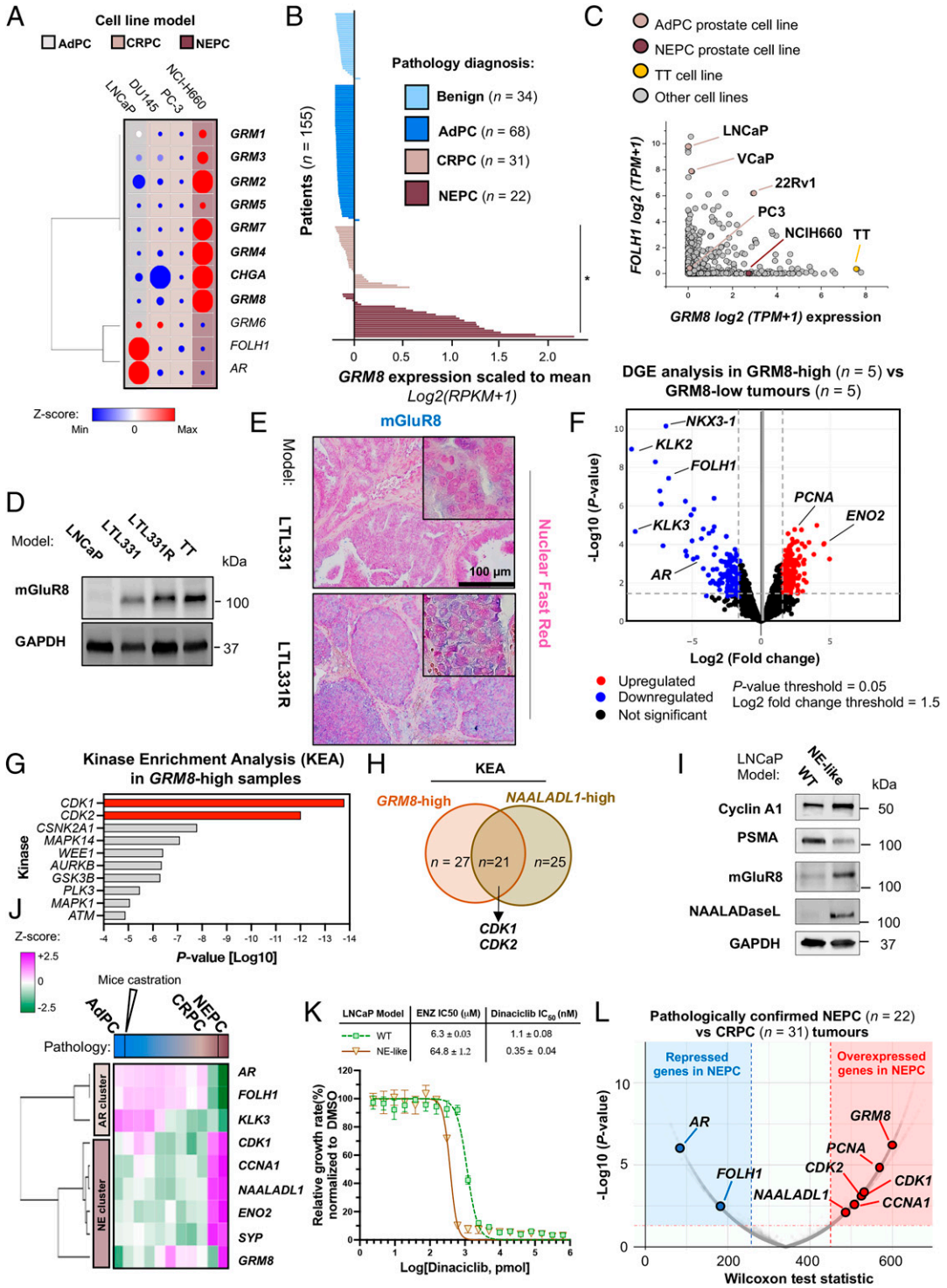

Fig. 3. Differential expression of *GRM* genes is associated with higher expression of NEPC markers and Cyclin A1, CDK1, and CDK2. (*A*) The heat map plot of the expression levels of *GRM*s levels in well-established prostate cell lines. (*B*) Waterfall plot of RNA-seq mGluR8 gene expression levels in different cohorts of prostate samples (*$P < 0.001$, Wilcoxon rank sum test). (*C*) The expression of *FOLH1* and *GRM8* in well-established cells lines ($n = 1,377$) of the DepMap 21Q3 dataset (39). (*D*) mGluR levels in LTL331 cell models were detected by immunoblotting. TT and LNCaP cell lines were used as mGluR8 positive and negative control samples, respectively. (*E*) Tissue sections of LTL331 models stained with nuclear fast red to visualize cell nuclei and blue chromogenic substrate used for detection of mGluR8. (*F*) A volcano plot of DGE analysis in *GRM8*-high ($n = 5$) vs. *GRM8*-low tumors ($n = 5$) in the SU2C/PCF Dream Team Dataset 2019 (40). The red points represent up-regulated differentially expressed genes, the blue points represent down-regulated differentially expressed genes, and the black points represent nondifferentially expressed genes. (*G*) Bar plot for the $\log_{10}$ of the *P* value of KEA in *GRM8*-high vs. *GRM8*-low tumors generated by the Enrichr tool (42). (*H*) Venn diagram illustrating the intersections between KEA data of *GRM8*-high and *NAALADL1*-high tumors. (*I*) Cyclin A1, PSMA, mGluR8, and NAALADaseL levels in LNCaP models were detected by immunoblotting. (*J*) Heat map plot of expression levels of *GRM8*, *NAALADL1*, *CCNA1*, and *CDK1* and their association with AR markers and NE markers in in PDX models. (*K*) Growth inhibition curves and IC_{50} of ENZ-sensitive LNCaP-WT and ENZ-resistant LNCaP-NE–like cell lines treated with CDK1/2 inhibitor (dinaciclib). (*L*) A plot of gene expression analysis in NEPC ($n = 22$) vs. CRPC ($n = 31$). *P* value threshold = 0.05.

A Synthetic Fluorescent Cy3-GUL Probe Is Predicted to Bind to All Three Proteins. The biochemical and computational data suggest that the GUL probes may interact well with mGluRs, especially mGluR8, and NAALADaseL, explaining their binding to PSMA-suppressed cells. To investigate this possibility histochemically we needed a fluorescent version of the GUL probe. To this end, we analyzed our predicted binding modes of F-GUL and Ga-GUL to design a cyanine dye-incorporating fluorescent probe (Cy3-GUL; *SI Appendix*, Fig. S25) analog of the clinical radiolabels (Fig. 4). A series of related probes with different linkers were computationally screened using induced-fit docking algorithms, but the best binding results were observed for a synthetically straightforward analog, Cy3-GUL, where a five-atom linker connects the GUL pharmacophore to the cyanine. This is a far closer connection than employed in either of the radiolabels but maintains the steric bulk at approximately the same distance from the GUL pharmacophore as F-GUL's naphthylalanine.

Comparing the predicted binding of Cy3-GUL with PSMA to that of Ga-GUL and F-GUL suggests that Cy3-GUL will adopt a similar pose to F-GUL, interacting with one of the Zn^{2+} ions through the P1″ carboxylate (Fig. 4*A* and Movie S7). Cy3-GUL forms fewer and less consistent hydrogen bonding interactions than the other probes, and like F-GUL (but unlike Ga-GUL), it does not enter the S1′ pocket; it also lacks F-GUL's imaging moiety, preventing the formation of a series of key interactions (*SI Appendix*, Fig. S2*C*). However, it does hydrogen bond to Arg534, Ser547, Tyr552, and Tyr700. As a result, greater root-mean-square deviation (RMSD) fluctuations occur for Cy3-GUL during the molecular dynamics (MD) simulation (*SI Appendix*, Fig. S4). Although more flexible, Cy3-GUL still forms enough key interactions to remain an excellent ligand for PSMA.

Cy3-GUL is predicted to bind very well to NAALADaseL with similar affinity as F-GUL and Ga-GUL (Fig. 4*C* and Table 1). The binding modes of all three probes are different due to the greater size of the NAALADaseL active site; however, they all bind with the GUL moiety extended into the binding pocket (Fig. 4*D* and Movie S8). In the case of Cy3-GUL, the P1″ carboxylate forms interactions with one of the Zn^{2+} ions (bound to P1 in Ga-GUL and P1′ in F-GUL). Several strong hydrogen bonds and salt bridges are formed with the receptor (Arg198, Arg539, Tyr544, and Gly195 backbone NH) which stabilize the complex and remain intact throughout the MD simulation. These are similar to those observed for F-GUL; however, F-GUL forms several additional interactions. Arg198 and Tyr544 are particularly important and form key interactions with all three probes (*SI Appendix*, Fig. S2*F*). Cy3-GUL again shows slightly greater fluctuation in the RMSD, largely due to the flexibility in the dye and linker domains due to their less charged nature.

Cy3-GUL shows stronger affinity for mGluR8 than for any of the other mGluRs (Fig. 4*E*, Table 1, and *SI Appendix*, Table S3), adopting a bound conformation distinct from that of the other two probes (Fig. 4*F* and Movie S9) with the GUL moiety buried deep within the highly charged cleft (Fig. 4*E*). Three extremely stable salt bridges are formed between the P1, P1′, and P1″ carboxylates and the Arg255, Arg188, and Arg255 of the second subunit (*SI Appendix*, Fig. S2*I*). Due to these key interactions, minimal RMSD fluctuations are observed in the MD simulation of the Cy3-GUL–mGluR8 complex. With both sufficient predicted binding and close agreement in the binding mode of the GUL pharmacophore to those of the clinical radiolabels, this probe was thus synthesized for in vitro evaluation, which we accomplished from a protected GUL moiety and our previously prepared cyanine dye (*SI Appendix*, Fig. S25 and accompanying discussion) (20).

Cy3-GUL Binds to PSMA In Vivo. Flow cytometry demonstrates far stronger uptake of Cy3-GUL into PSMA-positive LNCaP cells relative to PSMA-negative DU145 cells (*SI Appendix*, Fig. S26 *A* and *B*). This indicates that although Cy3-GUL is predicted to bind well to three different proteins, it is not generally promiscuous: it requires PSMA to bind the cell—both DU145 and LNCaP have low endogenous expression levels of both mGluRs and NAALADaseL (*SI Appendix*, Fig. S26*E*). In addition, the PSMA-positive LNCaP cells do not become fluorescent when they are exposed to the unconjugated dye, indicating the GUL moiety is essential for selective uptake (*SI Appendix*, Fig. S26*D*). Similarly, PSMA-negative DU145 cells, an AdPC cell line, show almost no Cy3-GUL uptake (*SI Appendix*, Fig. S26 *C* and *D*). Functionally, Cy3-GUL exposure shows no cytotoxicity to LNCaP or DU145 cells at any tested dose regardless of cell type (*SI Appendix*, Fig. S27). These data, along with the computational modeling, suggest that Cy3-GUL is an acceptable fluorescent homolog of the two clinically deployed PET reagents; we consequently used it to validate our hypothesis that GUL probes bind mGluR8 and NAALADaseL.

GUL Probes Are Selectively Taken Up by mGLuR and NAALADaseL. To investigate the affinity of GUL-based probes for mGluR8, we measured the uptake of Cy3-GUL into PSMA-negative DU145 cells both with and without overexpression of mGluR8 (Fig. 5 *A*–*C*). LNCaP-PSMA–positive cells were used as a positive control. The Cy3-GUL signal is predominantly localized to the cytoplasm. This is consistent with GUL-tracer localization; they are found both bound to PSMA at the membrane and internalized to the cytoplasm in a time-dependent fashion (45). Immunofluorescence microscopy demonstrates a fivefold increase in Cy3-GUL uptake when mGLuR8 was overexpressed (Fig. 5*C*). The involvement of mGluR8 is further supported by its up-regulation when PSMA-negative DU145 cells are driven to develop NE features by epidermal growth factor (EGF) and dibutyryl cAMP cotreatment and simultaneous serum starvation as previously described (Fig. 5*D* and *SI Appendix*, Fig. S28 *A* and *B*) (46). After treatment, cells display neuronal/neuroendocrine characteristics including neurite-like outgrowth (*SI Appendix*, Fig. S28*C*), while increasing their expression of select mGluR genes (including *GRM4* and *GRM8*) (*SI Appendix*, Fig. S28*C*). Similarly, differential expression of *GRM*s was observed following overexpression of *SRRM4* as a regulator of NEPC (*SI Appendix*, Fig. S29). Although not expressing PSMA, these cells still significantly increase their uptake of Cy3-GUL (Fig. 5*E*), supporting our hypothesis that GUL radiolabels may bind mGluRs such as mGluR8 and that these mGluRs could be markers of NEPC emergence.

To determine whether NAALADaseL can bind Cy3-GUL, we performed a knockdown of *NAALADL1* in WT LNCaP cells and LNCaP cells driven to a neuroendocrine phenotype (LNCaP-NE-like) after treatment with charcoal-stripped serum as previously described (17) (*SI Appendix*, Fig. S30 and Fig. 5 *F* and *G*). PCR analysis both confirmed the successful *NAALADL1* knockdown and demonstrated that *NAALADL1* gene expression is significantly higher in the LNCaP-NE-like line over control (Fig. 5*F*). When treated with the probe, Cy3-GUL uptake positively correlated with NAALADaseL levels. Cy3-GUL uptake was significantly reduced in LNCaP-NE cells with *NAALADL1* knockdown; however, probe uptake was unchanged in WT LNCaP cells despite successful knockdown (Fig. 5*G*). This is likely due to high PSMA expression in LNCaP control cells which was unaffected by *NAALADL1* knockdown (Fig. 5 *G* and *H*). To provide additional support that these effects were not due to some odd interaction with the dye rather than GUL, we further measured ^{68}Ga-PSMA-11 uptake in a variety of cell lines with different levels of PSMA, mGluR, and NAALADaseL. Fig. 5*I* shows Western blot analyses of PSMA levels in LNCaP and TT cell lines. For small interfering RNA (siRNA)-mediated *GRM8* and *NAALADL1* knockdown in TT cells, cells were transfected with either *NAALADL1* Smart Pool and/or *GRM8* Smart Pool or a nontargeting control siRNA (*SI Appendix*, Fig.

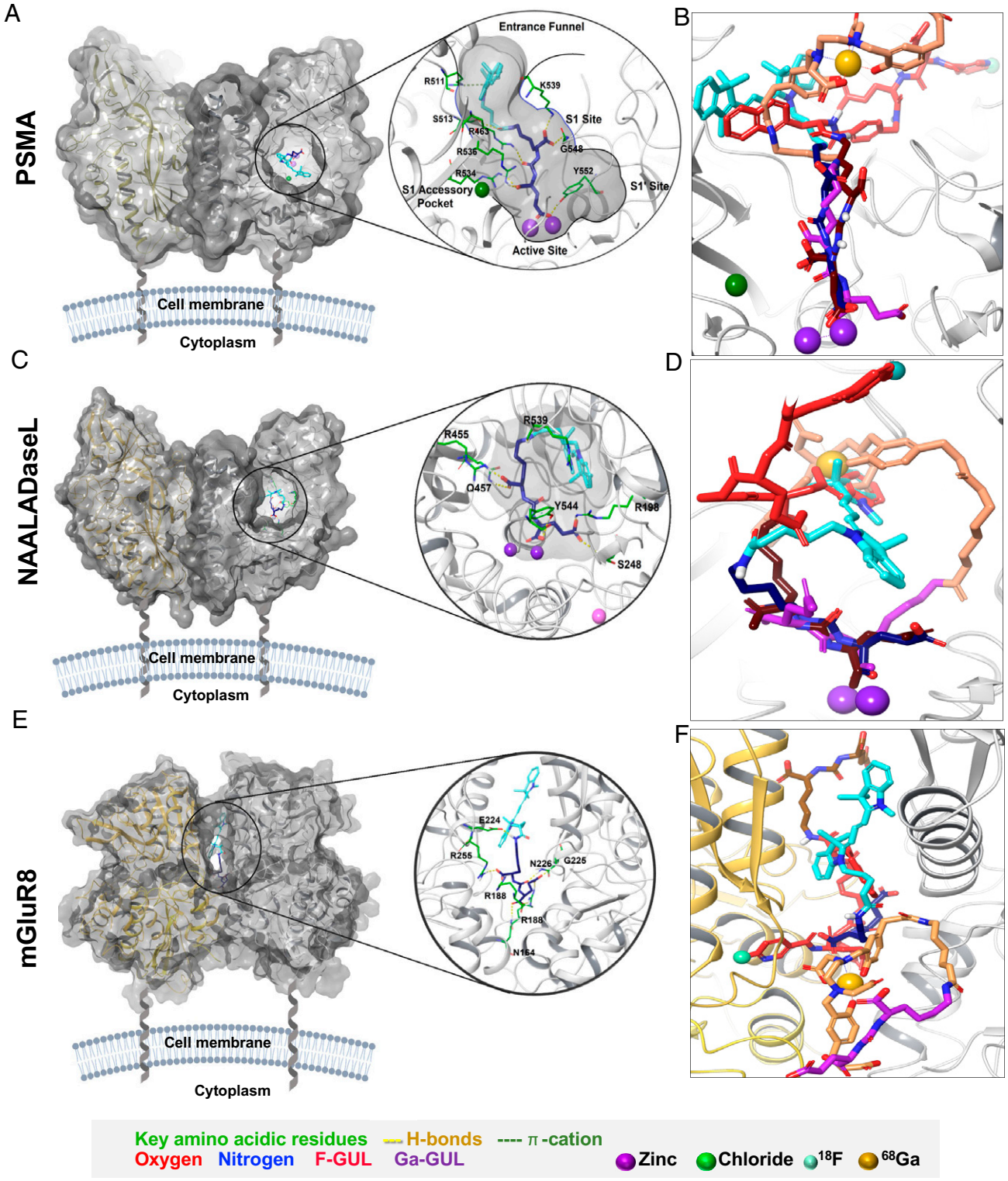

Fig. 4. Cy3-GUL probe binds to the PSMA and NAALADaseL active sites and mGluR8 cleft similar to the clinical radiopharmaceuticals. (*A*) Computed conformation of Cy3-GUL within the PSMA active site (*2XEG*). (*B*) Comparison of Cy3-GUL (GUL moiety in deep blue, dye in cyan), Ga-GUL (GUL moiety in maroon, ligand in red), and F-GUL (GUL moiety in purple, pseudopeptide in peach) within the PSMA active site. (*C*) Cy3-GUL's computed conformation within the NAALADaseL active site (*4TWE*). (*D*) Comparison of Cy3-GUL, Ga-GUL, and F-GUL in the NAALADaseL active site. Coloring is the same as in *B*. (*E*) Computed conformation of Cy3-GUL within the mGluR8 cleft (*6BSZ*). (*F*) Comparison of Cy3-GUL, Ga-GUL, and F-GUL in the mGluR8 cleft. Coloring is the same as in *B*.

S31). Normalized ^{68}Ga-PSMA-11 uptake in LNCaP and TT cell lines following inhibition of PSMA, mGluR8, and NAALADaseL is represented in Fig. 5*J*. As expected, ^{68}Ga-PSMA-11 uptake in LNCaP falls drastically upon PSMA inhibition. However, our known PSMA-negative TT cells have higher uptake of ^{68}Ga-PSMA-11 which implies the affinity of ^{68}Ga-PSMA-11 to PSMA-like proteins. Importantly, siRNA-mediated knockdown of both *GRM8* and *NAALADL1* in TT

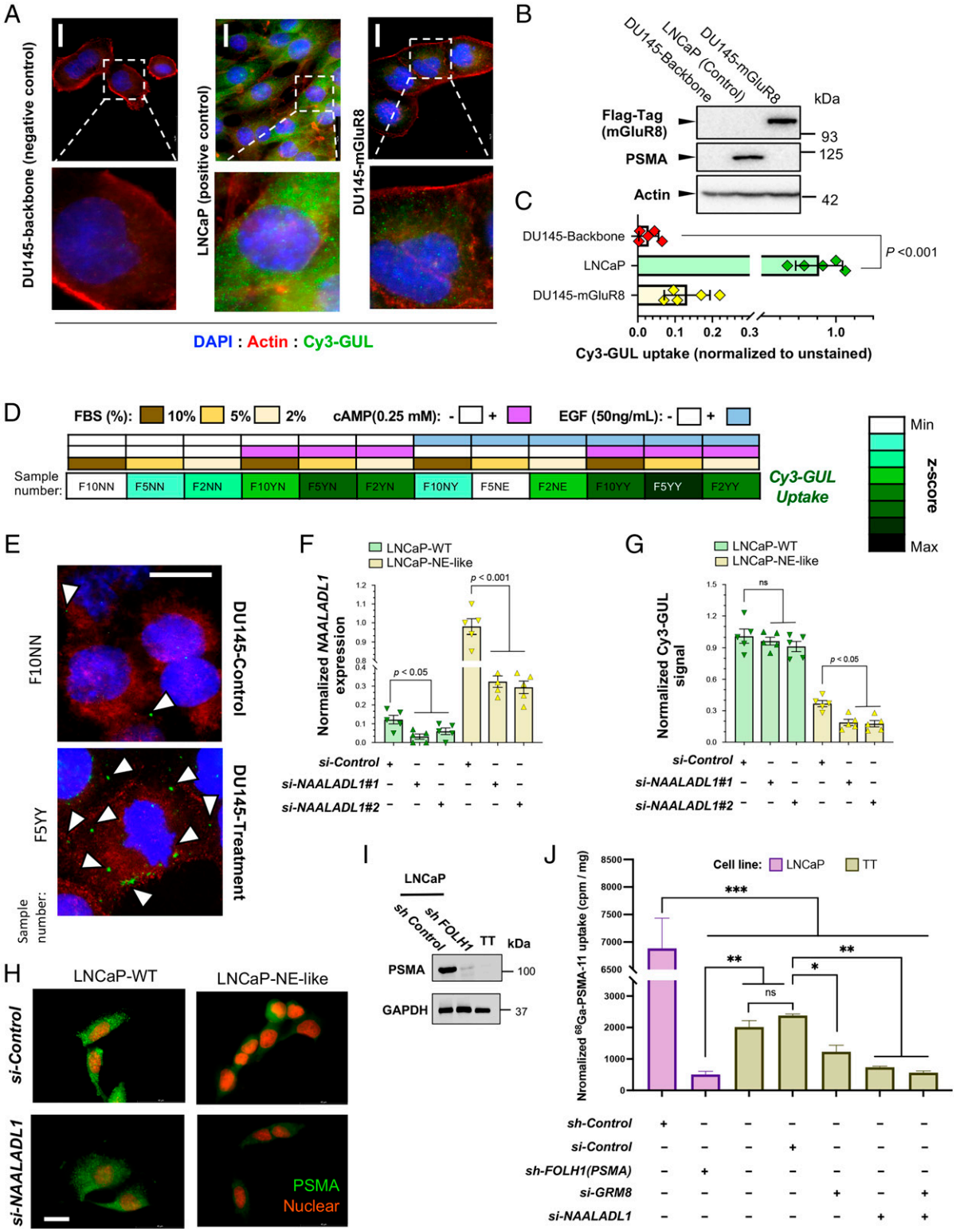

Fig. 5. NAALADaseL and mGluR8 regulate uptake of GUL-based tracers. The overexpression of mGluR8 in a PSMA-negative cell line induces uptake of Cy3-GUL. (*A*) Representative immunocytochemistry images of cells stained with Hoechst (blue), Cy3-GUL (green), and actin (red). (Scale bar, 20 μm.) (*B*) Western blot analyses of PSMA and mGluR8 protein levels. (*C*) Quantification of Cy3-GUL uptake, analyzed by one-way ANOVA. (*D*) NE transdifferentiation of DU145 cell line by EGF/cAMP treatment and serum starvation increases Cy3-GUL uptake. DU145 cell line was treated with cAMP (0.25 mM), EGF (50 ng/mL), and gradient levels of fetal bovine serum (FBS), while the control group (F10NN model) was treated with 10% FBS. Then after 3 d, the cells were incubated with 100 nM Cy3-GUL for 1 h and analyzed by PCR and immunocytochemistry. (*E*) Representative immunocytochemistry images of cells stained with Hoechst (blue), Cy3-GUL (green), and actin (red). The *NAALADL1* gene is up-regulated in the NE-like cell line model, and its inhibition could suppress GUL ligand uptake. (Scale bar, 20 μm.) (*F*) Quantification of *NAALADL1* gene expression using real-time PCR. (*G*) Quantification of Cy3-GUL uptake following inhibition of *NAALADL1* gene by flow cytometry. (*H*) Representative images of Cy3-GUL uptake in AdPC and NE-like models of LNCaP cell lines following inhibition of *NAALADL1* gene using siRNA technology. (Scale bar, 20 μm.) (*I*) Western blot analyses of PSMA levels in LNCaP and TT cells lines. (*J*) Normalized ^{68}Ga-PSMA-11 uptake in LNCaP and TT cell lines following inhibition of PSMA, mGluR8, and NAALADaseL. Cell uptake was expressed as counts per minute per milligram (cpm/mg) of total proteins. $*P < 0.05$, $**P < 0.01$ and $***P < 0.001$.

cells leads to suppression of ^{68}Ga-PSMA-11 nonspecific uptake. These two proteins appear to be excellent candidates for the non-PSMA binding of these GUL probes, and these experiments are also very much in line with the fluorescence dye data and the computational predictions. Cy3-GUL can be used in preclinical in vitro experiments as a nonradioactive PSMA tracer which demonstrates full binding capabilities of the GUL-based probes including the binding to PSMA-like proteins.

Conclusion

GUL-based probes are the state-of-the-art selective PSMA-targeting diagnostic tools, but emerging data show that they also bind to PSMA-negative prostate cancer tissues. Fortunately, these unknown target proteins do appear to be associated with prostate cancer, supporting that GUL-based probes function as multitargeting probes and are a benefit over approaches depending on antibody labels. The identities of these proteins were previously unknown and are of interest. As cells develop neuroendocrine features, both the *GRM*s and *NAALADL* genes are up-regulated while the gene encoding PSMA, *FOLH1*, levels fall. Our computational modeling suggested that the GUL probes should bind to the encoded proteins, consequently resulting in GUL probe recognition of PSMA-negative metastatic NEPC lesions. Fluorescent analog Cy3-GUL binds to these proteins, validating them as binding targets of GUL. Uptake of this and known radiochemical GUL probes depends on the presence of these proteins.

As important as the identification of these protein targets is, this project highlights the benefits of integrating computational and synthetic chemistry, with data mining of clinical databases and conducting in vitro and in vivo experiments to accelerate the validation of protein targets. This work explains why caution must be taken on clinical conclusions regarding treatment decisions made with PSMA-targeted imaging alone and suggests that mGluR and NAALADaseL may represent targets for imaging and therapeutic purposes. Paired probes may be useful for early detection of cancer progression to help inform treatment decisions. These proteins may play a role in NEPC, and their biochemical importance to this cancer deserves greater attention.

National Comprehensive Cancer Network (NCCN) Clinical Practice Guidelines in Oncology (NCCN Guidelines) currently recommend consideration of platinum-based chemotherapy regimens for NEPC. There is no known successful next line therapy for NEPC patients, particularly after platinum-based chemotherapy (47). AR independence and PSMA-negativity of NEPC have been a rationale for exclusion of PSMA-targeted therapy for NEPC tumors. In this work, we show GUL-targeted PET ligand can be used for imaging of PSMA-negative prostate cancers such as NEPC. This work supports the potential that PSMA-directed radiopharmaceuticals may also then target subsets of NEPC tumors with elevation of PSMA-like proteins mGluR8 and NAALADaseL. This would then make NEPC patients good candidates for some of the emerging PSMA-targeted clinical trials.

The mainstream clinical trials using CDK inhibitors for management of CRPC are focused predominantly on CDK4/6 inhibitors like palbociclib (48). This work shows that Cyclin D1 and CDK4/6 are not elevated with progression to NEPC; however, Cyclin A1 and partnering kinases CDK1/2 are significantly overexpressed in NEPC. We provide early evidence that NEPC shows sensitivity to the CDK1/2 specific inhibitor dinaciclib. This provides the exciting possibility that this could be a treatment avenue for the management of NEPC.

Methods

Cell Culture. All cell lines were purchased from the American Type Culture Collection (ATCC). *SI Appendix* includes the details of the culturing conditions. The LNCaP-NE–like cell line was derived by culturing LNCaP cells in RPMI1640 medium with 10% charcoal-stripped as previously characterized (20). LNCaP cells were treated with ENZ or dinaciclib (SCH727965) from Selleckchem.

Plasmids and Knockdown Experiments. GRM8-Tango was a gift from Dr. Bryan Roth (University of North Carolina, Chapel Hill, NC) (Addgene plasmid no. 66393) (49). For siRNA-mediated knockdown experiments, TT cells were transfected with Dharmacon Smart Pool according to the manufacturer's protocol. The listed siRNAs in *SI Appendix*, Table S1 were used for knockdown experiments of LNCaP cells. Transfections were performed using Lipofectamine 3000 (Life Technologies). Additional details of the experiments are provided in *SI Appendix*.

Immunoblotting, Immunocytochemistry, and Immunohistochemistry. *SI Appendix* includes a list of used antibodies. Immunoblotting and immunocytochemistry techniques were described previously (20). For immunohistochemistry, slide-mounted tissue sections were deparaffinized and developed in a fashion similar to that previously described (50) except that blue chromogenic substrate and nuclear fast red counterstain (Vector Laboratories) were used following diluted biotinylated secondary antibody (Jackson Immunoresearch Laboratories) and phosphatase avidin D (Vector Laboratories) incubation steps.

Cytotoxicity Evaluation and Cytometric Analysis. Cell viability was measured by methyl thiazolyl tetrazolium assay of Sigma-Aldrich according to the manufacturer's protocol. Cytometric analysis was performed using a BD LSRFortessa X-20 Flow Cytometer System.

Synthesis of Cy3-GUL and In Vitro Imaging. The chemical synthesis of a cyanine dye-incorporating fluorescent probe (Cy3-GUL) is summarized in *SI Appendix*, Fig. S25. *SI Appendix* includes synthetic chemistry experimental details. For the synthesis of the dye intermediates in *SI Appendix*, Fig. S25, please see our previous publication (20). For in vitro imaging, cells were seeded in 12-well dishes (Corning) overnight. Cells were treated with 100 nM Cy3-GUL and 100 ng/mL Hoechst 33342 (Thermo Scientific) for 5, 10, 30, 60, and 120 min. Cells were washed with phosphate buffered saline (PBS) and prepared for live imaging. *SI Appendix* contains additional imaging condition.

In Vitro ^{68}Ga-Labeled PSMA-11 Uptake Assay. As previously described (6), 48 h prior to the assay, cells were seeded in the 24-well plate. ^{68}Ga-labeled PSMA-11 (37 KBq) was added to each well. After 45 min incubation at 37 °C, cells were washed with ice-cold PBS, trypsinized and solutions were then collected for analysis by a gamma counter (Wizard^2; PerkinElmer). *SI Appendix* includes additional experimental details.

Data Mining and Gene Expression Analysis. DGE and KEA analyses were performed using BioJupies (51) and Enrichr (42) platforms. Kaplan–Meier plots and heat maps were generated using camcAPP (52), Broad Institute Morpheus software and R2: Genomics Analysis and Visualization Platform (http://r2.amc.nl). *SI Appendix* includes additional information about statistical analysis.

Computational Analyses. Docking was performed using the Glide (53) module of the Schrödinger suite. The MD simulations of the ligands were performed using Amber16 to study protein–ligand interactions and complex stability. *SI Appendix* includes additional information about MD protocol and preparation of protein and ligands.

PDX Models. We previously characterized and validated our PDX models as having AdPC and NEPC mRNA and protein signatures (41). The Institutional Review Board and Animal Care Committee of the University of British Columbia approved this study, and all subjects signed a written informed consent.

Data Availability. Data associated with the reported findings are available in the manuscript or supplementary information. Samples of the fluorescent Cy3-GUL probe are available on request while current supplies last for collaborative research purposes (contact J.F.T.).

ACKNOWLEDGMENTS. This study was supported by Canadian Institutes of Health Research Grants 142189 (L.A.P.), 141635, 144159, 153081, 173338 (Y.W.), and PJT156150 (X.D.), Natural Sciences and Engineering Research Council of Canada Grant 2018-06338 (J.F.T.), Government of Ontario Grant ER18-14-114 (J.F.T.), Windsor Cancer Centre Foundation Grant 2017-003 (J.F.T.), Canadian Tri-Council New Frontiers Exploration Fund Grant NFRFE-2018-00075 (J.F.T.), and the National Research Foundation of Korea (Grant 2020M2D9A1093988 to G.J.C.). The financial support of Telus Communications Company Ride for Dad, Prostate Cancer Fight Foundation (L.A.P.), Banting Research Foundation (J.F.T.), and Ontario Trillium Scholarship Program

(M.K.B.) is greatly appreciated. F.S.-R., D.M., and J.F.T. thank Compute Canada for providing the facilities of the Shared Hierarchical Academic Research Computing Network (http://www.sharcnet.ca) to support this project. Part of this work was supported by grants from the National Cancer Institute (NCI) to J.G. (NCI Grants CA257811 and R01 CA212379) and to the Memorial Sloan Kettering Cancer Center (Grant P30 CA08748).

1. R. L. Siegel, K. D. Miller, H. E. Fuchs, A. Jemal, Cancer statistics, 2021. *CA Cancer J. Clin.* **71**, 7–33 (2021).
2. S. Siva *et al.*, Expanding the role of small-molecule PSMA ligands beyond PET staging of prostate cancer. *Nat. Rev. Urol.* **17**, 107–118 (2020).
3. C. Zippel, S. C. Ronski, S. Bohnet-Joschko, F. L. Giesel, K. Kopka, Current status of PSMA-radiotracers for prostate cancer: Data analysis of prospective trials listed on ClinicalTrials.gov. *Pharmaceuticals (Basel)* **13**, 12 (2020).
4. W. G. Lesniak *et al.*, Evaluation of PSMA-targeted PAMAM dendrimer nanoparticles in a murine model of prostate cancer. *Mol. Pharm.* **16**, 2590–2604 (2019).
5. A. C. Baranski *et al.*, PSMA-11-derived dual-labeled PSMA inhibitors for preoperative PET imaging and precise fluorescence-guided surgery of prostate cancer. *J. Nucl. Med.* **59**, 639–645 (2018).
6. M. Eder *et al.*, 68Ga-complex lipophilicity and the targeting property of a urea-based PSMA inhibitor for PET imaging. *Bioconjug. Chem.* **23**, 688–697 (2012).
7. T. Ganguly *et al.*, A high-affinity [(18)F]-labeled phosphoramidate peptidomimetic PSMA-targeted inhibitor for PET imaging of prostate cancer. *Nucl. Med. Biol.* **42**, 780–787 (2015).
8. S. P. Rowe *et al.*, Prospective evaluation of PSMA-targeted 18F-DCFPyL PET/CT in men with biochemical failure after radical prostatectomy for prostate cancer. *J. Nucl. Med.* **61**, 58–61 (2020).
9. J. Kuten *et al.*, Head- to head comparison of ^{68}Ga-PSMA-11 with ^{18}F-PSMA-1007 PET/CT in staging prostate cancer using histopathology and immunohistochemical analysis as reference-standard. *J. Nucl. Med.* **61**, 527–532 (2020).
10. J. Cardinale *et al.*, Procedures for the GMP-compliant production and quality control of [^{18}F]PSMA-1007: A next generation radiofluorinated tracer for the detection of prostate cancer. *Pharmaceuticals (Basel)* **10**, 77 (2017).
11. C. Barinka *et al.*, Structural and computational basis for potent inhibition of glutamate carboxypeptidase II by carbamate-based inhibitors. *Bioorg. Med. Chem.* **27**, 255–264 (2019).
12. J. J. Vornov *et al.*, Looking for drugs in all the wrong places: Use of GCPII inhibitors outside the brain. *Neurochem. Res.* **45**, 1256–1267 (2020).
13. T. Maurer, M. Eiber, M. Schwaiger, J. E. Gschwend, Current use of PSMA-PET in prostate cancer management. *Nat. Rev. Urol.* **13**, 226–235 (2016).
14. C. Kaittanis *et al.*, Prostate-specific membrane antigen cleavage of vitamin B9 stimulates oncogenic signaling through metabotropic glutamate receptors. *J. Exp. Med.* **215**, 159–175 (2018).
15. M. K. Bakht *et al.*, Influence of androgen deprivation therapy on the uptake of PSMA-targeted agents: Emerging opportunities and challenges. *Nucl. Med. Mol. Imaging* **51**, 202–211 (2017).
16. M. C. Hupe *et al.*, Expression of prostate-specific membrane antigen (PSMA) on biopsies is an independent risk stratifier of prostate cancer patients at time of initial diagnosis. *Front. Oncol.* **8**, 623 (2018).
17. M. K. Bakht *et al.*, Neuroendocrine differentiation of prostate cancer leads to PSMA suppression. *Endocr. Relat. Cancer* **26**, 131–146 (2018).
18. H. Beltran *et al.*, Divergent clonal evolution of castration-resistant neuroendocrine prostate cancer. *Nat. Med.* **22**, 298–305 (2016).
19. E. G. Bluemn *et al.*, Androgen receptor pathway-independent prostate cancer is sustained through FGF signaling. *Cancer Cell* **32**, 474–489.e6 (2017).
20. M. K. Bakht *et al.*, Differential expression of glucose transporters and hexokinases in prostate cancer with a neuroendocrine gene signature: A mechanistic perspective for FDG imaging of PSMA-suppressed tumors. *J. Nucl. Med.* **61**, 904–910 (2020).
21. A. Paschalis *et al.*, Prostate-specific membrane antigen heterogeneity and DNA repair defects in prostate cancer. *Eur. Urol.* **76**, 469–478 (2019).
22. D. E. Spratt *et al.*, Utility of FDG-PET in clinical neuroendocrine prostate cancer. *Prostate* **74**, 1153–1159 (2014).
23. S. P. Thang *et al.*, Poor outcomes for patients with metastatic castration-resistant prostate cancer with low prostate-specific membrane antigen (PSMA) expression deemed ineligible for 177Lu-labelled PSMA radioligand therapy. *Eur. Urol. Oncol.* **2**, 670–676 (2019).
24. A. Iravani *et al.*, Molecular imaging of neuroendocrine differentiation of prostate cancer: A case series. *Clin. Genitourin. Cancer* **19**, e200–e205 (2021).
25. T. Derlin *et al.*, Neuroendocrine differentiation and response to PSMA-targeted radioligand therapy in advanced metastatic castration-resistant prostate cancer: A single-center retrospective study. *J. Nucl. Med.* **61**, 1602–1606 (2020).
26. K. Current *et al.*, Investigating PSMA-targeted radioligand therapy efficacy as a function of cellular PSMA levels and intra-tumoral PSMA heterogeneity. *Clin. Cancer Res.* **26**, 2946–2955 (2020).
27. W. P. Fendler *et al.*, PSMA PET Reader Group, False positive PSMA PET for tumor remnants in the irradiated prostate and other interpretation pitfalls in a prospective multi-center trial. *Eur. J. Nucl. Med. Mol. Imaging* **48**, 501–508 (2021).
28. S. Youn *et al.*, Carborane-containing urea-based inhibitors of glutamate carboxypeptidase II: Synthesis and structural characterization. *Bioorg. Med. Chem. Lett.* **25**, 5232–5236 (2015).
29. J. Pavlícek, J. Ptácek, C. Barinka, Glutamate carboxypeptidase II: An overview of structural studies and their importance for structure-based drug design and deciphering the reaction mechanism of the enzyme. *Curr. Med. Chem.* **19**, 1300–1309 (2012).
30. A. E. Machulkin *et al.*, Small-molecule PSMA ligands. Current state, SAR and perspectives. *J. Drug Target.* **24**, 679–693 (2016).
31. C. Barinka *et al.*, Interactions between human glutamate carboxypeptidase II and urea-based inhibitors: Structural characterization. *J. Med. Chem.* **51**, 7737–7743 (2008).
32. J. R. Mesters *et al.*, Structure of glutamate carboxypeptidase II, a drug target in neuronal damage and prostate cancer. *EMBO J.* **25**, 1375–1384 (2006).
33. A. X. Zhang *et al.*, A remote arene-binding site on prostate specific membrane antigen revealed by antibody-recruiting small molecules. *J. Am. Chem. Soc.* **132**, 12711–12716 (2010).
34. L. Y. Wu *et al.*, The molecular pruning of a phosphoramidate peptidomimetic inhibitor of prostate-specific membrane antigen. *Bioorg. Med. Chem.* **15**, 7434–7443 (2007).
35. Z. Novakova *et al.*, Unprecedented binding mode of hydroxamate-based inhibitors of glutamate carboxypeptidase II: Structural characterization and biological activity. *J. Med. Chem.* **59**, 4539–4550 (2016).
36. J. Cardinale *et al.*, Development of PSMA-1007-related series of ^{18}F-labeled Glu-ureido type PSMA inhibitors. *J. Med. Chem.* **63**, 10897–10907 (2020).
37. M. N. Pangalos *et al.*, Isolation and expression of novel human glutamate carboxypeptidases with N-acetylated α-linked acidic dipeptidase and dipeptidyl peptidase IV activity. *J. Biol. Chem.* **274**, 8470–8483 (1999).
38. M. J. Sippl, M. Wiederstein, Detection of spatial correlations in protein structures and molecular complexes. *Structure* **20**, 718–728 (2012).
39. D. Broad, *DepMap 21Q3 Public* (2021), 10.6084/m9.figshare.15160110.v2 (Accessed 12 August 2021).
40. W. Abida *et al.*, Genomic correlates of clinical outcome in advanced prostate cancer. *Proc. Natl. Acad. Sci. U.S.A.* **116**, 11428–11436 (2019).
41. S. Akamatsu *et al.*, The placental gene PEG10 promotes progression of neuroendocrine prostate cancer. *Cell Rep.* **12**, 922–936 (2015).
42. M. V. Kuleshov *et al.*, Enrichr: A comprehensive gene set enrichment analysis web server 2016 update. *Nucleic Acids Res.* **44**, W90–W97 (2016).
43. B. S. Taylor *et al.*, Integrative genomic profiling of human prostate cancer. *Cancer Cell* **18**, 11–22 (2010).
44. C. H. Yam, T. K. Fung, R. Y. C. Poon, Cyclin A in cell cycle control and cancer. *Cell. Mol. Life Sci.* **59**, 1317–1326 (2002).
45. M. Schottelius *et al.*, Synthesis and preclinical characterization of the PSMA-targeted hybrid tracer PSMA-I&F for nuclear and fluorescence imaging of prostate cancer. *J. Nucl. Med.* **60**, 71–78 (2019).
46. S. Humez *et al.*, Epidermal growth factor-induced neuroendocrine differentiation and apoptotic resistance of androgen-independent human prostate cancer cells. *Endocr. Relat. Cancer* **13**, 181–195 (2006).
47. Y. Yamada, H. Beltran, Clinical and biological features of neuroendocrine prostate cancer. *Curr. Oncol. Rep.* **23**, 15 (2021).
48. P. L. Palmbos *et al.*, A randomized phase II study of androgen deprivation therapy with or without palbociclib in RB-positive metastatic hormone-sensitive prostate cancer. *Clin. Cancer Res.* **27**, 3017–3027 (2021).
49. W. K. Kroeze *et al.*, PRESTO-Tango as an open-source resource for interrogation of the druggable human GPCRome. *Nat. Struct. Mol. Biol.* **22**, 362–369 (2015).
50. J. E. Stark *et al.*, Juvenile OLFM4-null mice are protected from sepsis. *Am. J. Physiol. Renal Physiol.* **318**, F809–F816 (2020).
51. D. Torre, A. Lachmann, A. Ma'ayan, BioJupies: Automated generation of interactive notebooks for RNA-seq data analysis in the cloud. *Cell Syst.* **7**, 556–561.e3 (2018).
52. M. J. Dunning *et al.*, Mining human prostate cancer datasets: The "camcAPP" Shiny App. *EBioMedicine* **17**, 5–6 (2017).
53. R. A. Friesner *et al.*, Glide: A new approach for rapid, accurate docking and scoring. 1. Method and assessment of docking accuracy. *J. Med. Chem.* **47**, 1739–1749 (2004).